BMBAD BJESR Mühendislik Bilimleri ve Araştırmaları Dergisi
Journal of Engineering Sciences and Researches

Effect of Anodic Polarization and Sliding Wear on Pitting Corrosion Behavior of Shipbuilding Aluminum Alloy 5083

Anodik Polarizasyon ve Kayma Aşınmasının Gemi İnşa Alüminyum Alaşımı 5083'ün Çukurcuk Korozyonu Davranışına Etkisi

[1]Sabri ALKAN

[1]Bandırma Onyedi Eylül Üniversitesi, Denizcilik Meslek Yüksekokulu, Bandırma/Balıkesir, Türkiye

[1]salkan@bandirma.edu.tr

Araştırma Makalesi/Research Article

ARTICLE INFO

Article history

Received : 4 August 2023
Accepted : 10 September 2023

Keywords:

Aluminum Alloy, Shipbuilding, Corrosive Wear, Pitting Corrosion, Tribocorrosion

ABSTRACT

This study aimed to characterize the pitting corrosion and simultaneous wear-corrosion (tribocorrosion) mechanisms of shipbuilding aluminum alloy 5083 under sliding wear and different anodic polarization conditions in simulated seawater. A tribocorrosion experimental setup was provided for the study under a 3 N load and different anodic potentials in a 3.5% NaCl solution. In the study, many grooves, parallel scratches and transverse cracks were determined on the wear track surface due to the low hardness of the test material. The corrosion rate of AA5083 increased nearly seven-fold in sliding tribocorrosion conditions than in corrosion conditions under open circuit potential. Chloride ions played a decisive role in the corrosion and tribocorrosion behavior of AA 5083. The dissolution of AA5083 increased from open circuit potential to higher anodic potentials. A half-cube mechanism, similar to the pitting corrosion of pure aluminum were observed under high anodic potentials.

MAKALE BİLGİSİ

Makale Tarihleri

Gönderim : 4 Ağustos 2023
Kabul : 10 Eylül 2023

Anahtar Kelimeler:

Alüminyum Alaşım, Gemi İnşa, Korozif aşınma, Çukurcuk Korozyonu, Tribokorozyon

ÖZET

Bu çalışma, simüle edilmiş deniz suyunda kayma aşınması ve farklı anodik polarizasyon koşulları altında gemi yapımında kullanılan alüminyum alaşımı 5083'ün çukurcuk korozyonu ve eş zamanlı aşınma-korozyon (tribokorozyon) mekanizmalarını karakterize etmeyi amaçladı. Çalışma için %3.5 NaCl çözeltisinde 3 N yük ve farklı anodik potansiyeller altında bir tribokorozyon deney düzeneği sağlanmıştır. Çalışmada, test malzemesinin sertliğinin düşük olması nedeniyle aşınma izi yüzeyinde çok sayıda oluk, paralel çizik ve enine çatlak tespit edilmiştir. AA5083'ün korozyon hızı, kaymalı tribokorozyon koşullarında, açık devre potansiyeli altındaki korozyon koşullarına göre neredeyse yedi kat arttı. AA 5083'ün korozyon ve tribokorozyon davranışında klorür iyonları belirleyici bir rol oynadı. AA5083'ün bozunması açık devre potansiyelinden daha yüksek anodik potansiyellere gittikçe arttı. Yüksek anodik potansiyeller altında, saf alüminyumun çukurcuk korozyonuna benzer bir yarım küp mekanizması gözlendi.

ORCID ID: [1]0000-0002-1052-4778

1. INTRODUCTION

The most effective way to limit greenhouse gas emissions in the maritime industry is to lighten the structure during ship design and construction to reduce fuel consumption [1]. So, in recent years, shipyards have shifted to using aluminum alloys (AAs) to achieve weight savings in high-speed ferries, patrol boats, yachts, and offshore wind service vessels [2–7]. This way, weight saving can provide almost half of a similar steel hull structure [8,9]. Moreover, AAs, as well as lightness, have excellent corrosion resistance in marine environments. They can form a few nanometers thick oxide film on their surface almost instantaneously [10,11], significantly protecting bare metal from the environment. Thus, thanks to the passive oxide film, the material surface rarely comes into direct contact with the environment. However, the oxide film may deteriorate [10,12] if there is continuous mechanical action while in an electrolyte, such as in ship-ice interaction [13–17] or underwater friction stir welding [2,18,19]. During ship-ice interaction or underwater friction stir welding, different material degradation mechanisms trigger each other, and a non-reversible material deterioration can emerge due to a combination of wear and corrosion, namely tribocorrosion [20,21].

In tribocorrosion, sliding wear and electrochemical potential can direct material loss and corrosion behavior [12,22,23]. Although aluminum alloys have excellent corrosion resistance in seawater, they are sensitive to pitting corrosion in aqueous media like other passive metals [24–30]. In marine environments, chloride ions provide an incredible convenience in approaching the metal surface due to their small size when the oxide film deteriorates [24,31,32]. Gulbransen [11] explained that the oxide film protectivity by the Pilling-Bedworth Ratio that the oxide film can shield defects nearly 3-4 nm in size [12,22]. The structure of the oxide film is affected to varying degrees by different parameters such as oxygen pressure, temperature, surface condition of the metal and alloying element additions [19,33]. Alloying elements significantly influence the OCP of aluminum alloys and can vary the potential in both directions [34]. Magnesium is a critical alloying element with higher diffusion characteristics than aluminum, resulting in the formation of MgO for aluminum-magnesium alloys [35].

Aluminum alloys are grouped into eight series [27]. The variety of alloys explains the expansion of applications with a comprehensive range of specific characteristics, such as tensile strengths varying from 100 to 700 MPa [6,36]. While AAs exhibit different properties in each series, they typically have similar properties in the same series, such as cast ability, extrudability, wear and corrosion [6]. Shipyards mostly prefer the strain-hardened (H) tempers of 5XXX series aluminum alloys (aluminum-magnesium alloys) with the highest formability for ship structures, heat exchangers, seawater desalination, or subsea robotics, which could contact seawater [5,7,36–38]. The mechanical properties of the shipbuilding aluminum (aluminum-magnesium) alloys increase as almost linear as a function of magnesium content up to 7 wt.% magnesium for wrought alloys and up to 12 wt.% for casting alloys. However, it evolved that higher magnesium content leads to susceptibility to intergranular pitting and stress corrosion [26,30,39,40]. Alloying elements, additives, and impurities affect AAs' chemical design, which directs mechanical properties [27], such as hardness, wear and frictional characteristics [18,41]. In contrast to their excellent corrosion resistance, the low mechanical strength of aluminum alloys makes them vulnerable to tribocorrosion [28].

In the shipbuilding industry, aluminum alloys are extensively utilized, but limited knowledge exists about how anodic polarization and sliding wear impact pitting corrosion and tribocorrosion in seawater for AA5083. Understanding the wear and corrosion behavior of shipbuilding aluminum alloys such as hull-ice interactions in seawater frictional conditions is pivotal. Addressing this gap, the study probes the pitting corrosion and tribocorrosion of AA5083 under anodic polarization and sliding wear in seawater, revealing the intricate alloy-environment interplay for the first time. While aluminum alloys are increasingly favored for ship weight reduction and corrosion resistance, the nuanced relationship between wear, corrosion, and alloy traits remains insufficiently explored. The novelty of this study stems from its holistic investigation into the multifaceted interactions among sliding wear, electrochemical potentials, and corrosion mechanisms in a marine context.

2. MATERIALS AND EXPERIMENTS

2.1. Materials

AA5083 plates were used in this study because of their extensive use in shipbuilding applications. The chemical properties are presented in Table 1, and Table 2 shows the mechanical properties of the materials used in the study. The samples were extracted from 0.5 mm thickness plates of AA5083. Their dimensions were 23 mm x 10 mm, so the bare surface of the samples was 2.3 cm^2 in the corrosion and tribocorrosion tests which will be in contact with the electrolyte. A shielded electrical cable was soldered back of the samples to get electrochemical data during the corrosion and tribocorrosion tests. Afterwards, the samples were embedded into Bakelite to contact only the test surface with the electrolyte. The AA5083 samples were treated with acetone under ultrasonic cleaning for 15 min. The bare surface of the samples in Bakelite was polished with emery papers of 600–1500 mesh. The samples were polished to get a mirror-like finish with 1 µm Al_2O_3 solutions. Finally, they were cleaned with deionized water and ethanol and dried with hot air.

Table 1. Chemical composition of AA5083.

Material	Elements (Content-Wt. %) (min.-max.)									
	Fe	Si	Mn	Cr	Ti	Cu	Mg	Zn	Other	Al
AA5083	0.4	0.4	0.4-1.0	0.05-0.25	0.15	0.1	4-4.9	0.25	0.15	Rem.

Table 2. Mechanical properties of AA5083.

Material	Mechanical Properties				
	Temper	**Yield strength (MPa)**	**Tensile strength (MPa)**	**Elongation (%)**	**Hardness (HB)**
AA5083	H111	125-145	275-300	22	70-75

2.2. Experiments and Investigation Methods of Surface Morphology

The experimental setup used in the study is presented in Figure 1. A potentiostat combined with a linear reciprocating type tribometer (Turkyus-Turkey) was used to collect the electrochemical data during sliding tribocorrosion tests. The corrosion cell and ball holder were produced from Delrin to prevent unwanted corrosion effects during the tests. A 3.5% wt NaCl solution was prepared in each trial, and 100 ml electrolyte was filled into the corrosion cell.

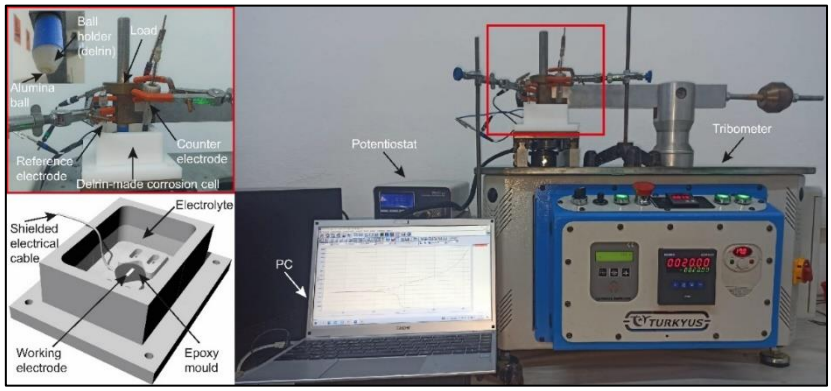

Figure 1. Tribocorrosion experimental setup [42].

The sintered alumina (Al_2O_3) ball with a diameter of 6.35 mm and 14 GPa hardness was used as an abrasive counter body. The wear stroke was 6 mm, and a linear motion speed of 0.02 m/s during 1200 s was achieved in tribocorrosion tests. A load of 3 N was chosen to simulate the frictional force that occurs during marine structural aluminium alloy applications [13], such as ship-ice interaction or underwater robotics [14–17]. OCPs were measured for 1 hour before all tests. Ag/AgCl electrode was used as a reference electrode (RE), platinum as a counter electrode (CE), and aluminium alloy samples were used as the working electrode (WE) in the study. The Zive SP1-type analyzer test devices were used with a standard three-electrode system in the electrochemical experiments. The Zive Data Manager software was used to obtain electrochemical data. The ASTM G5-14 standard was followed to describe corrosion potential (E_{corr}) and current density (I_{corr}). Potentiodynamic polarization tests varied from −1 V to +1 V on both electrochemical and triboelectrochemical conditions at a scan rate of 1 mV/s. The cyclic polarisation scans were also conducted further to investigate the pitting corrosion susceptibility of AA5083. The anodic tribocorrosion tests were conducted at constant potentials on AA5083 samples. The anodic potentials of −400 mV, −600 mV and −900 mV were applied according to polarisation curves concerning OCPs to understand the dissolution of the alloy. Filmetrics Profilm 3D-Germany laser scanning microscope was used to define the surface morphology of the track after tribocorrosion tests. MAIA3, XMU model SEM instrument also analyzed the detail surface characteristics with its EDS (OXFORD, X-Max model) capability.

3. RESULTS AND DISCUSSIONS

3.1. Effect of Sliding Wear on Electrochemical Potential

Fig. 2 shows the change in OCP of AA5083 in a 3.5% NaCl solution for 6000 s both corrosion and sliding wear conditions. In Fig. 2, changes in OCP were characterized in four regions. After the alloy contacted the electrolyte, the electrochemical potentials increased almost linearly during in 600 s immersion period in the first region. The potential was stabilized after that period during 3000 s, and sliding started at the end of the second period. In the third region, OCP decreased from -724 mV to nearly -1150 mV due to the deterioration of the passive layer. Mechanical contact caused a shift to the negative direction in electrochemical potential because of the deterioration in the protective oxide layer [43]. The deterioration due to sliding in the wear track caused the formation of an anodic region. In this case, unworn regions with their deformed passive layer behaved as cathodic regions, and a battery cell occurred because of the potential difference [20,44,45]. This result caused a negative shift in OCP

[46]. In the fourth region, as soon as the sliding is finished, the surface starts to passivate itself again. Finally, a steady state condition in potential was achieved nearly after 5000 s in Fig. 2 [47].

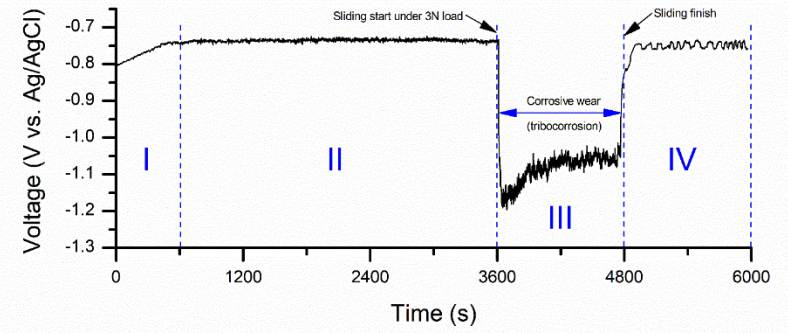

Figure 2. Variation in open circuit potential of AA5083 with time.

3.2. Potentiodynamic and Cyclic Polarization Scans

Fig. 3 shows potentiodynamic polarization scans employed for understanding corrosion kinetics under different electrochemical states. Tafel polarization curves were used to get the electrochemical data are shown in Table 3 for AA5083 under corrosion and 3 N sliding tribocorrosion conditions in 3.5% NaCl. The mechanical effects shifted the corrosion potential negatively in Fig. 3. The electrochemical behavior of AA5083 aluminum samples during polarization changed under sliding conditions due to the impairment of the oxide film by the load [20]. The shifting of OCP to the negative direction is a classical reaction of all passive alloys during polarization in a seawater environment [27,46,48]. The OCP of AA5083 was −724 mV under corrosion conditions and decreased to −1175 mV under tribocorrosion conditions. However, the corrosion rates of AA5083 increased under tribocorrosion conditions due to wear and corrosion synergism which can be induced by each other [44,49].

The combined action of mechanical wear and electrochemical processes creates an environment conducive to localized material loss, often resulting in more aggressive degradation compared to individual wear or corrosion scenarios. The observed increase in corrosion rate under sliding conditions can be attributed to the removal of the protective oxide layer, exposing fresh metal surfaces to the corrosive electrolyte [20]. This phenomenon is further compounded by the synergistic effects of mechanical wear, which not only physically removes material but also disrupts the passivating oxide layer, allowing aggressive ions to penetrate and exacerbate the corrosion process [31]. The distinct shifts in corrosion potential and corrosion rate emphasize the significance of tribocorrosion phenomena in real-world scenarios involving mechanical interaction within corrosive environments. The findings underscore the necessity of considering both mechanical and electrochemical aspects when evaluating the durability and performance of materials in practical applications, particularly in maritime environments where tribocorrosion can play a pivotal role in material degradation.

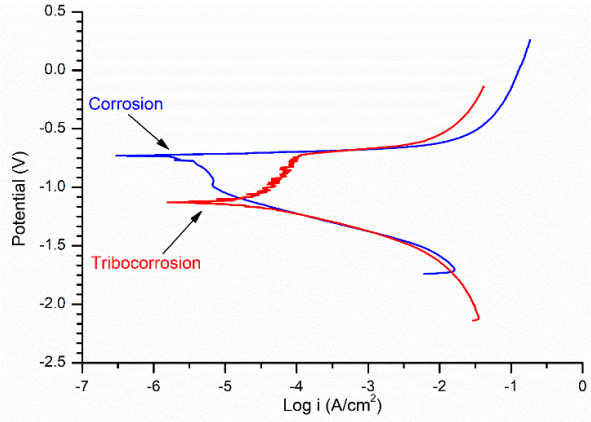

Figure 3. Potentiodynamic polarization curves.

Table 3. Potentiodynamic polarization data of AA5083 under corrosion and tribocorrosion states in 3.5% NaCl.

Parameters	Corrosion	Tribocorrosion
E_{corr} (mV)	-724	-1175
β_a	0.013	0.673
β_c	0.210	0.033
I_{corr} (A/cm^2)	3.462E-6	2.249E-5
R_p (kOhm)	1.609	0.620
Corrosion rate (mmpy)	0.037	0.245

Fig. 4 presents the cyclic potentiodynamic polarization (CPDP) curves of AA5083 obtained in the study. The susceptibility of metals to localized corrosion can be evaluated in a short time by the CPDP technique [50]. It is an extended curve of potentiodynamic polarization with a reverse scan. In the forward scan of CPDP curves in Fig. 4, the beginning of the immediate increase of the corrosion current represents the pitting potential (E_{pit}) and conforms to the initial collapse of the passive film and the following stabilization of one or more corrosion pits [31]. Several parameters complicate the susceptibility of pitting corrosion examination.
Moreover, the potential at which the development rate of the pits stops is called the repassivation potential (E_{rp}). It indicates that the passive surface is irreparable if it is more active than the corrosion potential (E_{corr}). During scanning, the point where the backward polarization curve intersects with the forward polarization curve is called protection potential (E_{pp}). E_{pp} is the lowest point of the anodic current density in the backward polarization scanning. The resistance of a material to localized corrosion is assessed based on the E_{rp} measurement to the E_{corr}. If E_{rp} runs into the more noble values than the E_{corr}, the propagation of active pits is reduced or eliminated. Therefore, the passive film is stable at the potentials between the Epp and E_{corr}, and no pits will start or develop. This part of the curve is named perfect passivity. Only old pits propagate at the potential between the E_{pit} and E_{pp}, and no new pits nucleate. If E_{corr} fits between E_{pit} and E_{rp}, the repassivation of pits will not occur, and preformed pits will continue to develop and reproduce [51].
Hysteresis in the CPDP curve can supply data on pitting corrosion and how readily a passive film restores itself. The difference between $E_{pit} - E_{rp}$ (amount of hysteresis) indicates the localized corrosion amount. If the current density in the reverse scan exceeds the forward scanning curve, it will indicate pitting corrosion. Negative hysteresis emerges when the current density of the reverse scan is less than that of the forward, and positive hysteresis emerges when the current density of the reverse scan is more significant than that of the forward. A positive hysteresis loop was detected at the high potential of scan reversal, meaning the specimen experienced localized corrosion. Fig. 4 shows a slight positive hysteresis in the CPDP curves for AA5083. In Fig. 4, the E_{corr} value of AA5083 was −1278 mV. E_{pit} value was about −700 mV. However, there was a remarkable variation between the absolute difference of the E_{corr} and E_{rp} values of the alloys, which mainly determines the pitting corrosion resistance ($R_{pit} = | E_{corr} - E_{pit} |$). The absolute difference between the E_{corr} and E_{rp} values of AA5083 indicates higher pitting corrosion resistance and the amount of localized corrosion. It should also be noted that as a result of cyclic polarization, degradation in the surface occurred, and this caused a slight change in corrosion potential.

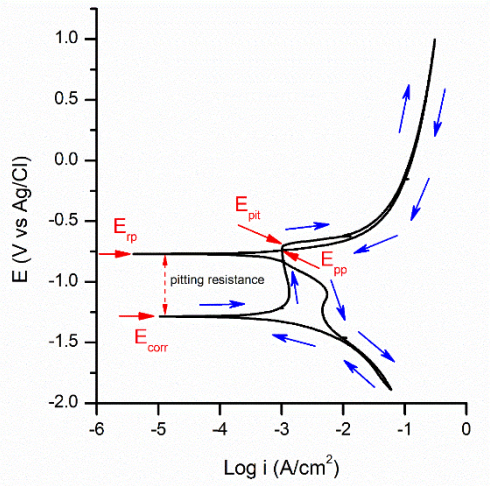

Figure 4. Cyclic polarization scans for AA5083 under 3 N sliding condition in chloride solution.

3.3. Tribocorrosion Tests under Constant Anodic Potentials and Coefficient of Friction

Potentiostatic tribocorrosion tests were performed to examine the wear and corrosion behaviors of AA5083 at different constant potentials under 3 N sliding conditions. Anodic potentials of −400 mV, −600 mV and −900 mV was selected and employed according to polarization curves in the experiment series. Fig. 5 represents the current trends registered at anodic potentials after sliding starts during 1200 s for AA5083 in simulated seawater. The current value is zero under the OCP since no current will flow through the circuit before the sliding starts. In Fig. 5, the current values are positive for anodic potentials and prove the anodic dissolution of the alloy [26]. The current fluctuations indicate the electrochemical activity within the wear track.
Fig. 6 shows the change in COF values during sliding potentiostatic tests. The COF values performed nearly similar behavior with time for AA5083 with an increasing trend, and the results were also compatible with previous studies [10,33]. The creation of third bodies may cause an increase in the COF with the continuous surface change due to the sliding. The fact that AA5083 has a lower hardness than the alumina ball caused it to undergo easy plastic deformation under high tribological contact.

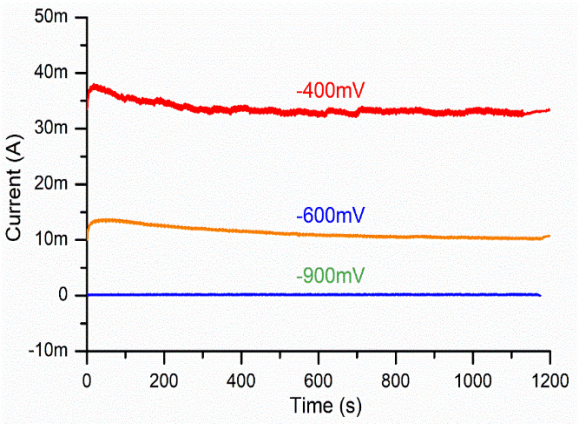

Figure 5. The current change during potentiostatic tribocorrosion tests.

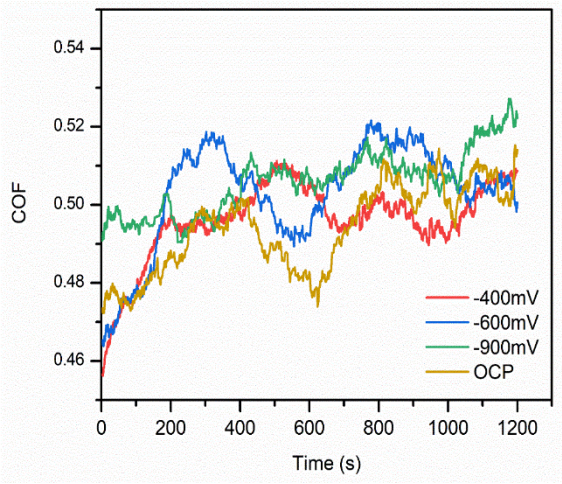

Figure 6. COF changes over time under different electrochemical sliding conditions in NaCl solution.

3.4. Surface Morphology Analysis and Pitting Corrosion Investigations

The surface morphology and tribocorrosion mechanism of the samples were investigated by optical and SEM after tribocorrosion tests. Optical microscope images of the wear track morphologies obtained under different triboelectrochemical conditions were presented in Fig. 7. The pits in the unworn region of anodic samples were more apparent in Fig. 7. However, the wear track morphology of the OCP sample has narrower and less deep than the abraded anodic samples. Figure 8 depicts optical micrographs of anodically polarized samples under −400 mV, −600 mV, −900 mV and OCP. Clustered pits were identified on the -400-mV anodic sample surface in Fig. 8a, and they were nearly 80 microns in diameter under -600 mV anodic potential in Fig. 8b.

SEM images of the wear tracks under different electrochemical sliding states were presented in Fig. 9. Abrasive effects were evident for all samples. Parallel scratches to the sliding direction and cracks in the wear track were pronounced. The dense pitting presence in the unworn areas, especially under anodic potentials of -400 mV and -600 mV, indicates galvanic coupling between wear track and non-abraded surfaces in Fig. 9. In Fig.9, It was determined that pitting corrosion does not occur in a region near the wear track (indicated by orange arrows) in the -400 mV and -600 mV samples. The width of this region increases when passing from -400 mV to -600 mV and disappears with pits in -900 mV and OCP samples. This finding may be related to anodic current changes.

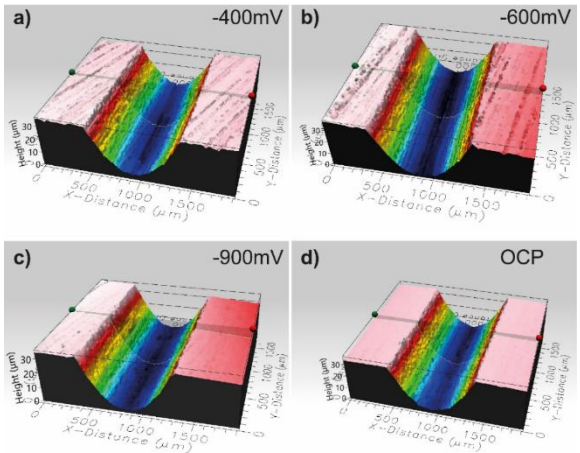

Figure 7. Wear track cross-sections after tribocorrosion tests a) -400 mV, b) -600 mV, c) -900 mV, d) OCP.

Fig. 10 presents the EDS mapping of the OCP sample after the test. Elemental distribution in worn and unworn surfaces was identified in Fig. 10a. The rubbed area was oxidized, and Cl ions were evident on the sample surface, mainly in the wear track. This determination is significant because Cl ion concentration directly affects intergranular and pitting corrosion initiation and propagation. Small Cl ions can easily penetrate the passive protective oxide film on the aluminum alloys and degrade the oxide protection mechanism on the surface [31]. Fig. 10b also shows the map sum spectrum and validates the leakage of Cl ions and oxide formation on the sample's surface. The pits on the unworn surface are also identified and seen in Fig. 10b.

Fig. 11 represents SEM images of the wear track and unworn surfaces of AA5083 samples after the tribocorrosion test conducted under open circuit and anodic potentials. When Figure 11 was analyzed, pits were evident in the unworn regions at higher anodic potentials, especially −400 mV and −600 mV. In the wear tracks of the samples,

there were many parallel scratches to the sliding direction, micro-grooves, and cracks resulting from the sliding of the hard alumina counter body.

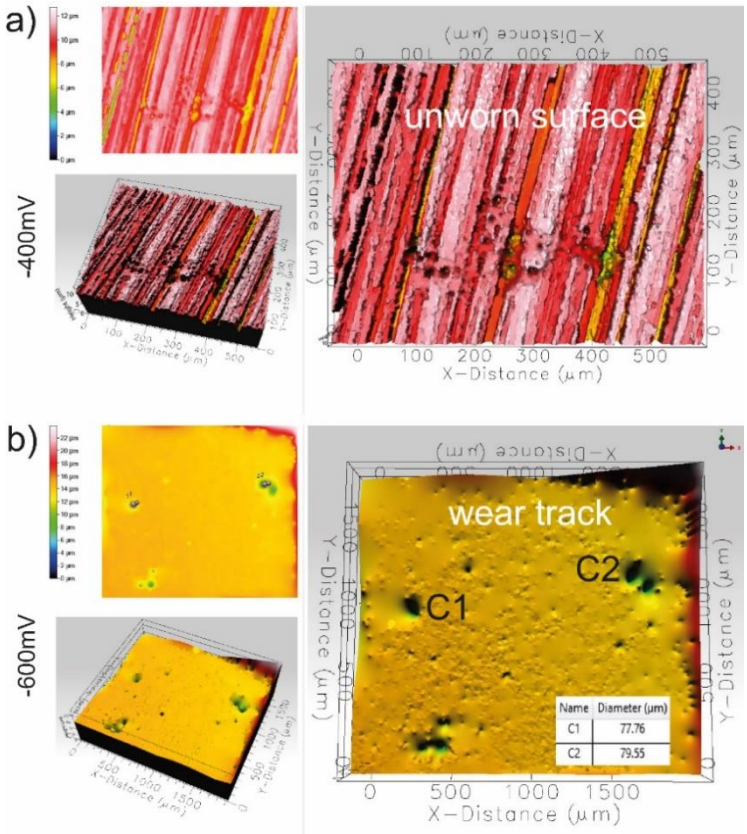

Figure 8. Optical microscope images of determined pits under anodic potentials a) -400 mV, b) -600 mV.

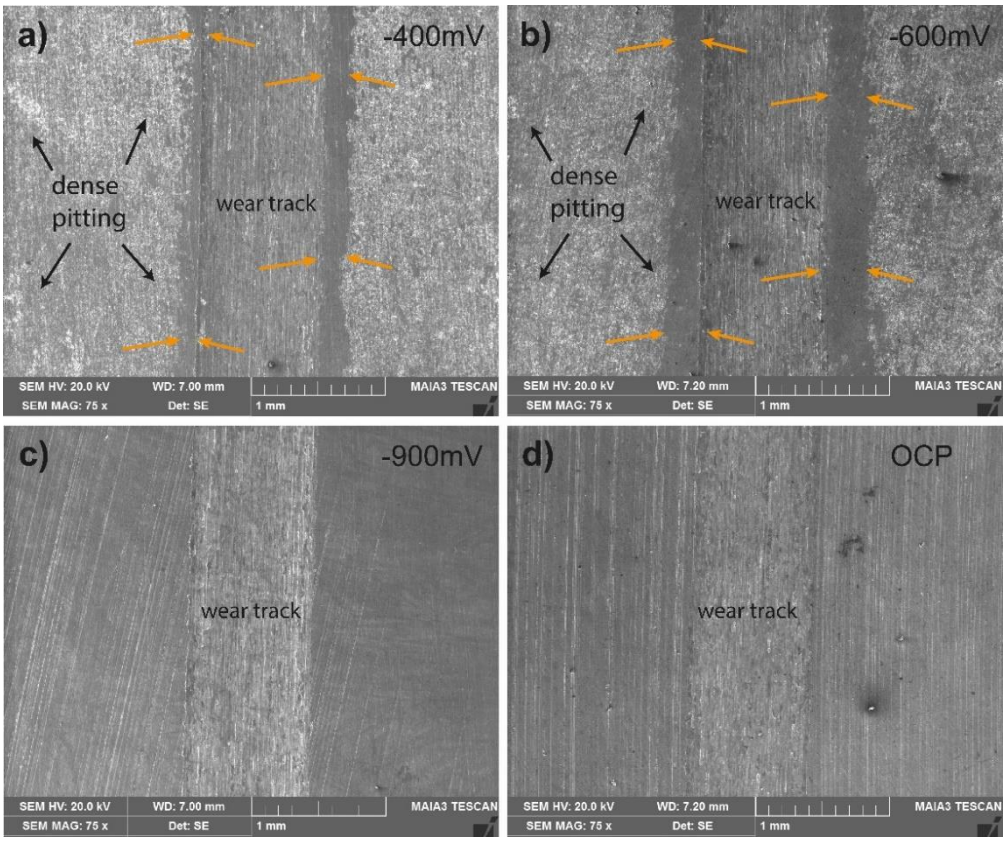

Figure 9. SEM images of wear tracks after tribocorrosion tests a) -400 mV, b) -600 mV, c) -900 mV, d) OCP.

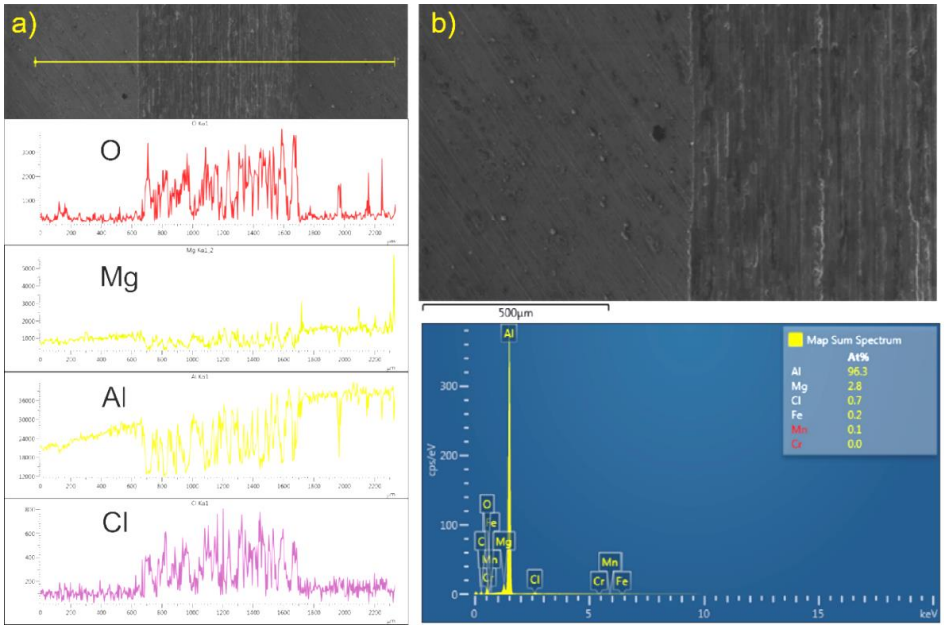

Figure 10. EDS analysis of OCP sample a) line spectrum, b) map sum spectrum.

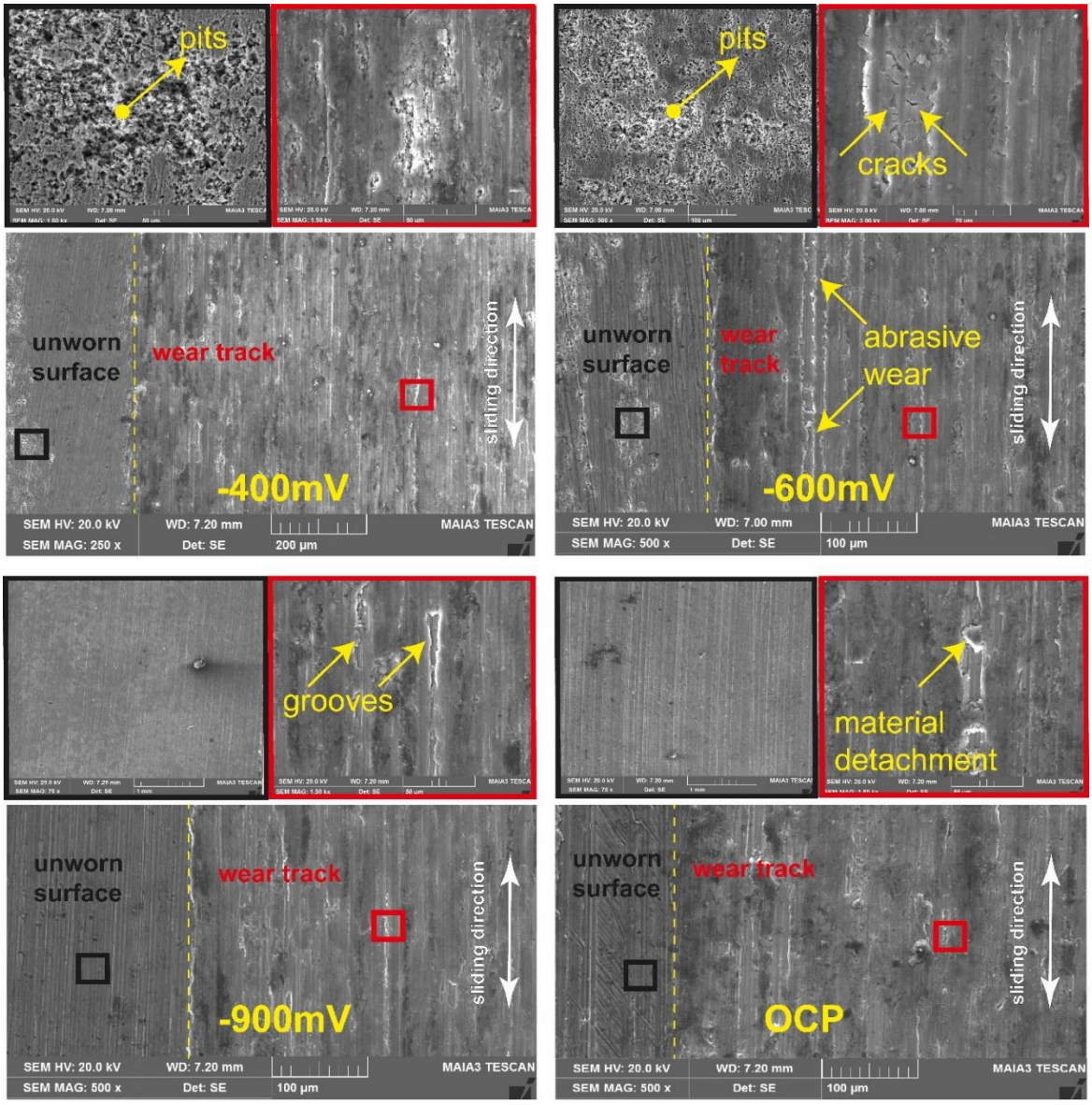

Figure 11. SEM images of worn and unworn surfaces after OCP and anodic tribocorrosion tests.

Several researchers showed an intergranular to pitting corrosion transformation mechanism under anodic potentials in marine environments [5,25,30,52]. They have reported that corrosion of the alloy first occurs at the grain boundary, and after the grain boundary is attacked, corrosion propagates into the grain as a source of crystallographic pitting [25,52,53]. This transformation mechanism is notably depicted in Fig. 12, wherein the observed half-cube mechanism is attributed to intergranular pitting corrosion, a phenomenon tightly linked to the cubic lattice structure of the alloy. Analogous observations have been reported by researchers in the realm of aluminum corrosion, thus corroborating the broader applicability of such mechanisms [52,54]. This interplay between grain boundaries, lattice structure, and the localized corrosion process highlights the intricacies inherent in alloy degradation under complex environmental and mechanical conditions. It further underscores the necessity of a nuanced understanding of corrosion mechanisms to inform effective strategies for alloy design and mitigation of degradation processes in practical applications.

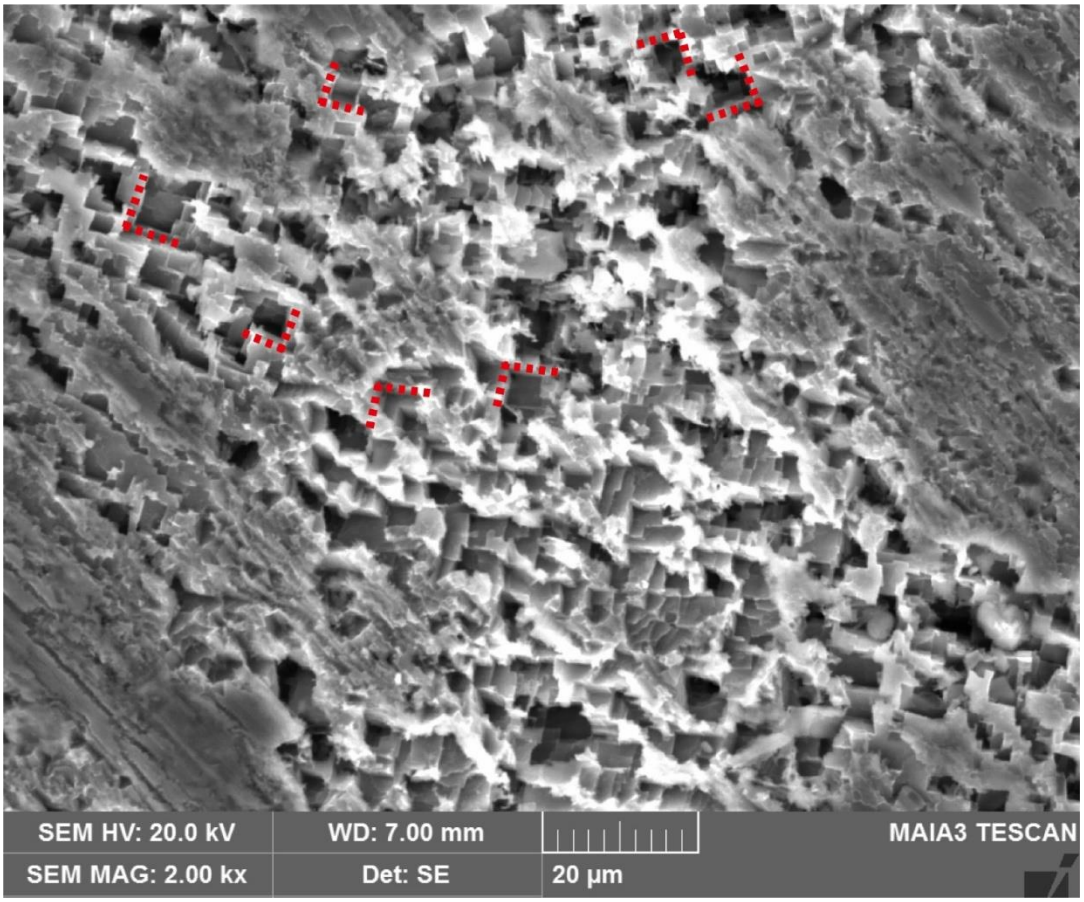

Figure 12. Half cube pitting corrosion mechanism under anodic potential of -400 mV.

4. CONCLUSIONS

The study assessed the corrosion and tribocorrosion response of AA5083 under a 3 N load in 3.5% NaCl solution, observing decreased open circuit potential (OCP) due to passive oxide layer degradation during sliding tribocorrosion. Enhanced wear track features, including grooves, parallel scratches, and transverse cracks, were evident. Alloying elements and particularly Cl ions exerted a decisive influence on corrosion behavior. The study revealed that the corrosion rate of AA5083 exhibited an approximate seven-fold increase under sliding tribocorrosion conditions compared to corrosion conditions at open circuit potential. The study also identified an intergranular pitting corrosion mechanism resembling the half-cube mechanism of pure aluminum. As aluminum alloys gain prominence for their weight-saving and corrosion-resistant attributes in maritime contexts, comprehending the intricate interplay of wear, electrochemistry, and corrosion mechanisms becomes pivotal. This study's revelation of AA5083's vulnerability to pitting and intergranular stress corrosion, attributed to alloy composition, serves as a guide for optimizing alloy designs to bolster mechanical robustness and corrosion resistance. By addressing this critical knowledge gap through a comprehensive exploration of wear-corrosion interactions in marine environments, the study facilitates the formulation of effective strategies aimed at enhancing material performance, durability, and sustainability in the maritime domain. These findings have the potential to guide the shipbuilding sector by offering vital insights into the wear-corrosion dynamics of AA5083 under anodic polarization and sliding wear in seawater.

Author Contributions

All stages of the study were done by the author.

Conflict of Interest

The author declares that there is no conflict of interest.

KAYNAKÇA

[1] T. Lamb "Concepts for Ferry Propulsion and Emissions Performance Improvement," J. Sh. Prod. Des., vol. 31, no. 03, pp. 170–180, 2015.

[2] M.O.M. Segaetsho, V. Msomi, and V. Moni "Corrosion behaviour of friction stir welded dissimilar joints produced from AA5083 and other alloys of aluminium: A critical review," Mater Today Proc., vol. 56, pp. 1696–1701, 2022.

[3] C. Wei, G. Wang, M. Cridland, D.L. Olson, and S. Liu "Corrosion protection of ships", Third Edit. Elsevier Inc., 2018.

[4] B. Ertuğ and C. Kumruoğlu "5083 type Al-Mg and 6082 type Al-Mg-Si alloys for ship building," Am. J. Eng. Res., vol. 4, no. 3, pp. 146–150, 2015.

[5] J. Liu, M.J. Tan, A.E. W. Jarfors, Y. Aue-u-lan, and S. Castagne "Formability in AA5083 and AA6061 alloys for light weight applications," Mater. Des., vol. 31, no. SUPPL. 1, pp. S66–S70, 2010.

[6] C. Vargel, Corrosion of Aluminium. Elsevier, 2004.

[7] K.E. Perumal, "Handbook of Environmental Degradation of Materials", Elsevier, 2012.

[8] S. Gupta, D. Singh, A. Yadav, S. Jain, and B. Pratap "A comparative study of 5083 aluminium alloy and 316L stainless steel for shipbuilding material," Mater Today Proc., vol. 28, pp. 2358–2363, 2020.

[9] T.S. Um and M.Il Roh "Optimal dimension design of a hatch cover for lightening a bulk carrier," Int. J. Nav. Archit. Ocean Eng., vol. 7, no. 2, pp. 270–287, 2015.

[10] Z. Li, H. Yu, and D. Sun "The tribocorrosion mechanism of aluminum alloy 7075-T6 in the deep ocean," Corros. Sci., vol. 183, no. August 2020, p. 109306, 2021.

[11] E.A. Gulbransen and W.S. Wyong "Thin oxide films on aluminum," J. Phys. Colloid Chem., vol. 51, no. 5, pp. 1087–1103, 1947.

[12] E.P. Georgiou et al. "Effect of cathodic hydrogen charging on the wear behavior of 5754 Al alloy," Wear, vol. 390–391, pp. 295–301, 2017.

[13] H. Wu et al. "Influences of Load and Microstructure on Tribocorrosion Behaviour of High Strength Hull Steel in Saline Solution," Tribol. Lett., vol. 67, no. 4, pp. 1–12, 2019.

[14] I. Kubat, M. Sayed, and A. Collins "Modeling of Pressured Ice Interaction with Ships," SNAME 9th International Conference and Exhibition on Performance of Ships and Structures in Ice. p. D021S004R002, Sep. 20, 2010.

[15] J.H. Kim and Y. Kim "Numerical simulation on the ice-induced fatigue damage of ship structural members in broken ice fields," Mar. Struct., vol. 66, no. March, pp. 83–105, 2019.

[16] M. Kotilainen, J. Vanhatalo, M. Suominen, and P. Kujala "Predicting ice-induced load amplitudes on ship bow conditional on ice thickness and ship speed in the Baltic Sea," Cold Reg. Sci. Technol., vol. 135, pp. 116–126, 2017.

[17] F. Li, M. Kõrgesaar, P. Kujala, and F. Goerlandt "Finite element based meta-modeling of ship-ice interaction at shoulder and midship areas for ship performance simulation," Mar. Struct., vol. 71, no. August 2019, 2020.

[18] N.R. Ramesh and V.S.S. Kumar "Experimental erosion-corrosion analysis of friction stir welding of AA 5083 and AA 6061 for sub-sea applications," Appl. Ocean Res., vol. 98, no. September 2019.

[19] I.A. Kartsonakis, D.A. Dragatogiannis, E.P. Koumoulos, A. Karantonis, and C.A. Charitidis, "Corrosion behaviour of dissimilar friction stir welded aluminium alloys reinforced with nanoadditives," Mater. Des., vol. 102, pp. 56–67, 2016.

[20] A C. Vieira, L.A. Rocha, N. Papageorgiou, and S. Mischler "Mechanical and electrochemical deterioration mechanisms in the tribocorrosion of Al alloys in NaCl and in NaNO3 solutions," Corros. Sci., vol. 54, no. 1, pp. 26–35, 2012.

[21] R.J.K. Wood "Marine wear and tribocorrosion," Wear, vol. 376–377, pp. 893–910, 2017.

[22] K. Wang, Y. Wang, X. Yue, and W. Cai "Multiphysics modeling and uncertainty quantification of tribocorrosion in aluminum alloys," Corros. Sci., vol. 178, no. November 2020, p. 109095, 2021.

[23] V.I. Pokhmurskii, I.M. Zin, V.A. Vynar, and L.M. Bily "Contradictory effect of chromate inhibitor on corrosive wear of aluminium alloy," Corros. Sci., vol. 53, no. 3, pp. 904–908, 2011.

[24] B. Grgur and L. Marunkić "The influence of chloride anions on the pitting corrosion of aluminum alloy en 46000," Zast. Mater., vol. 59, no. 2, pp. 243–248, 2018.

[25] J. Ress, U. Martin, J. Bosch, R.K. Gupta, and D.M. Bastidas "Intergranular to intragranular pitting corrosion transition mechanism of sensitized aa5083 at 150°c," Metals (Basel)., vol. 10, no. 8, pp. 1–21, 2020.

[26] Y.J. Yang and S.J. Kim "Electrochemical characteristics of aluminum alloys in sea water for marine environment," Acta Phys. Pol. A, vol. 135, no. 5, pp. 1005–1011, 2019.

[27] H. Ezuber, A. El-Houd, and F. El-Shawesh "A study on the corrosion behavior of aluminum alloys in seawater," Mater. Des., vol. 29, no. 4, pp. 801–805, 2008.

[28] G. Meyer-Rodenbeck, T. Hurd, and A. Ball "On the abrasive-corrosive wear of aluminium alloys," Wear, vol. 154, no. 2, pp. 305–317, 1992.

[29] C.N. Panagopoulos and E.P. Georgiou, "The effect

of hydrogen charging on the mechanical behaviour of 5083 wrought aluminum alloy," Corros. Sci., vol. 49, no. 12, pp. 4443–4451, 2007.

[30] L. Tan and T.R. Allen "Effect of thermomechanical treatment on the corrosion of AA5083," Corros. Sci., vol. 52, no. 2, pp. 548–554, 2010.

[31] S. Alkan "Evaluation of pitting susceptibility and tribocorrosion behaviors of AISI 304 stainless steel in marine environments," Proc. Inst. Mech. Eng. Part J J. Eng. Tribol., 2022.

[32] S. Alkan and M.S. Gök "Influence of plasma nitriding pre-treatment on the corrosion and tribocorrosion behaviours of PVD CrN, TiN and AlTiN coated AISI 4140 steel in seawater," Lubr. Sci., vol. 34, no. 2, pp. 67–83, 2022.

[33] H. Mraied and W. Cai "The effects of Mn concentration on the tribocorrosion resistance of Al – Mn alloys," Wear, vol. 380–381, pp. 191–202, 2017.

[34] A. International "Corrosion: Environments and Industries," in ASM Handbook, ASM International, 2006.

[35] K. Shimizu, G.M. Brown, K. Kobayashi, P. Skeldon, G.E. Thompson, and G.C. Wood "The early stages of high temperature oxidation of an Al-0.5 wt% Mg alloy," Corros. Sci., vol. 40, no. 4–5, pp. 557–575, 1998.

[36] O.F. Hosseinabadi and M. R. Khedmati "A review on ultimate strength of aluminium structural elements and systems for marine applications," Ocean Eng., vol. 232, no. April, p. 109153, Jul. 2021.

[37] K.R. Chasse, A.J. Scardino, and G.W. Swain "Corrosion and fouling study of copper-based antifouling coatings on 5083 aluminum alloy," Prog. Org. Coatings, vol. 141, no. August 2019, p. 105555, 2020.

[38] D. Kumar, J. Jain, and N.N. Gosvami "Macroscale to Nanoscale Tribology of Magnesium-Based Alloys: A Review," Tribol. Lett., vol. 70, no. 1, pp. 1–29, 2022.

[39] Y. Tzeng, R. Chen, and S. Lee "Nondestructive tests on the effect of Mg content on the corrosion and mechanical properties of 5000 series aluminum alloys," Mater. Chem. Phys., vol. 259, no. September 2020, p. 124202, 2021.

[40] H. Kamoutsi, G.N. Haidemenopoulos, V. Bontozoglou, and S. Pantelakis "Corrosion-induced hydrogen embrittlement in aluminum alloy 2024," Corros. Sci., vol. 48, no. 5, pp. 1209–1224, 2006.

[41] M. Szkodo, A. Stanisławska, A. Komarov, and Ł. Bolewski "Effect of MAO coatings on cavitation erosion and tribological properties of 5056 and 7075 aluminum alloys," Wear, vol. 474–475, no. September 2020, 2021.

[42] S. Alkan "Enhancement of Marine Corrosion and Tribocorrosion Resistance of Offshore Mooring Chain Steel By Aluminizing Process," Brodogradnja, vol. 73, no. 4, pp. 131–159, 2022.

[43] N. Papageorgiou and S. Mischler "Electrochemical simulation of the current and potential response in sliding tribocorrosion," Tribol. Lett., vol. 48, no. 3, pp. 271–283, 2012.

[44] Y.H. Liew, C. Örnek, J. Pan, D. Thierry, S. Wijesinghe, and D.J. Blackwood "Towards understanding micro-galvanic activities in localised corrosion of AA2099 aluminium alloy," Electrochim. Acta, vol. 392, p. 139005, 2021.

[45] K.C. Tekin and U. Malayoglu "Assessing the tribocorrosion performance of three different nickel-based superalloys," Tribol. Lett., vol. 37, no. 3, pp. 563–572, 2010.

[46] S. Alkan and M.S. Gök "Effect of sliding wear and electrochemical potential on tribocorrosion behaviour of AISI 316 stainless steel in seawater," Eng. Sci. Technol. an Int. J., vol. 24, no. 2, pp. 524–532, 2021.

[47] J. Zahavi and M. Metzger "Electron Microscope Study of Breakdown and Repair of Anodic Films on Aluminum," J. Electrochem. Soc., vol. 119, no. 11, p. 1479, 1972.

[48] A. Bidiville, M. Favero, P. Stadelmann, and S. Mischler "Influence of Applied Potential on the Mechanical Response of Stainless Steel During Tribocorrosion," ECS Meet. Abstr., vol. MA2007-02, no. 13, pp. 853–853, 2007.

[49] B. Zhang, J. Wang, and F. Yan "Load-dependent tribocorrosion behaviour of nickel-aluminium bronze in artificial seawater," Corros. Sci., vol. 131, no. December 2016, pp. 252–263, 2018.

[50] S. Esmailzadeh, M. Aliofkhazraei, and H. Sarlak "Interpretation of Cyclic Potentiodynamic Polarization Test Results for Study of Corrosion Behavior of Metals: A Review," Prot. Met. Phys. Chem. Surfaces, vol. 54, no. 5, pp. 976–989, 2018.

[51] W.S. Tait "Electrochemical corrosion basics," Handb. Environ. Degrad. Mater. Third Ed., pp. 97–115, 2018.

[52] X. Zhang, X. Zhou, T. Hashimoto, and B. Liu "Localized corrosion in AA2024-T351 aluminium alloy: Transition from intergranular corrosion to crystallographic pitting," Mater. Charact., vol. 130, no. May, pp. 230–236, 2017.

[53] M. Chen, Y. Deng, J. Tang, S. Fan, and X. Zhang "A study of the crystallographic pitting behavior of Al-0.54Mg-0.66Si aluminum alloy in acidic chloride solutions," Mater. Charact., vol. 148, no. December 2018, pp. 259–265, 2019.

[54] K. Jafarzadeh, T. Shahrabi, S.M.M. Hadavi, and M. G. Hosseini "Morphological characterization of AA5083-H321 aluminum alloy corrosion in NaCl solution under hydrodynamic conditions," Anti-Corrosion Methods Mater., vol. 56, no. 1, pp. 35–42, 2009.